ORIGINAL ARTICLE

Strong form meshfree collocation method for frictional contact between a rigid pile and an elastic foundation

Ashkan Almasi[1] · Tae-Yeon Kim[2] · Jeong-Hoon Song[1]

Abstract

In this paper, a strong form meshfree collocation method is developed for two-dimensional single-body frictional contact problems. In this approach, a point-wise Taylor series approximation and generalized moving least squares approach is used to construct numerical differential operators at discrete points within the domain. The differential operators are then used to spatially discretize and solve the governing partial differential equations. Contact constraint conditions are formulated with the penalty approach. To demonstrate the efficiency of the method, benchmark problems in frictionless and frictional contact relevant to a rigid pile and an elastic foundation contact are provided. The numerical results are also compared with the finite element solutions to verify robustness and accuracy of the method.

1 Introduction

The importance of computational contact mechanics in engineering applications has grown considerably over the past few decades. Contributions from research in this field of study have produced robust and efficient methods with increased accuracy to predict mechanical contact phenomena. However, due to the complicated non-linear phenomena inherent in contact problems, achieving robust predictions remains an elusive endeavor. At present, many approaches to contact are built on traditional weak-form-based finite element methods (FEM), mortar element method and boundary element method (BEM). For instance, there are nite element formulations dealing with large deformation contact problems that are based on master/slave contact strategies. Hallquist et al. [1] proposed the two- and three-dimensional contact algorithm in large-scale lagrangian computations. Simo et al. [2] developed a nite element procedure for

contact problems for the general case of fully nonlinear kinematics. Benson and Hallquist [3] introduced a contact algorithm that requires only a single surface definition for its analysis. Papadopoulos and Taylor [4] presented a nite element algorithm for the fully non-linear two-dimensional kinematics applicable to contact problems involving large deformations. Wriggers et al. [5] introduced a finite element method for contact using a third medium that is based on a space filling mesh in which the contacting bodies can move and interact.

The mortar element method [6–9] is a domain decomposition-based discretization technique that adopted variational discretizations across subdomain boundaries. The mortar method presents the continuity condition at the contact interfaces in global form, rather than as local constraints. One of the key advantages of the mortar element method is handling various types of nonconformities with great flexibility such as functional nonconformity, geometrical nonconformity, and overlapping nonconformity. Furthermore, the mortar nite element method preserves optimal convergence rates compare to the conventional nite element method based on contact analysis method [10]. The mortar element method has been applied to various frictional contact problems [11–16].

The overhead incurred from processes associated with these methods, i.e. mesh generation and numerical integration corresponds to reduction in computation efficiency.

✉ Jeong-Hoon Song
jh.song@colorado.edu

[1] Department of Civil, Environmental and Architectural Engineering, University of Colorado at Boulder, Boulder, CO 80309, USA

[2] Civil Infrastructure and Environmental Engineering, Khalifa University of Science and Technology, Abu Dhabi 127788, UAE

Moreover, using adaptive refinement on the contact region is not an easy task. To deal with such difficulties, this study proposes a strong form meshfree collocation method [17–19] which is constructing high order interpolants and its derivatives at discrete collocation points based on the moving least-square approximations of the Tylor expansion. However, it is worth mentioning that an idea was initially introduced by other researchers such as moving least squares (MLS) approximation [20–22] and reproducing kernel (RK) approximation [23–28] for the meshfree methods. Recently, the proposed method has been applied to various engineering problems such as strong and weak discontinuities problems [17, 18] and moving interface problem [19], dynamic crack propagation problem [29], polycrystalline growth problems [30–32], inelastic material problems [33], and ocean circulation problem [34]. The main goal of this study is introducing a strong form meshfree collocation methods and its application for frictionless and frictional engineering problems.

Several meshfree methods for solving contact problems have been developed in recent years. Chen and Wang [35] proposed new boundary condition treatments to enhance the computational efficiency of meshfree methods for contact problems. Li and Belytschko [36] introduced the formulation of the element-free Galerkin method for large displacements and contact problems. Xiao et al. [37] developed a subdomain variational and its meshless linear complementary formulation for solving two-dimensional contact problems.

Several Isogeometric collocation methods have been proposed recently. De Lorenzis et al. [38] presented a contact formulation for isogeometric analysis collocation (IGA-C) method. Kruse et al. [39] introduced the application of IGA-C method for large deformation elasticity and frictional contact problems. Weeger et al. [40] presented IGA-C method for the rod structures subject to large deformation and rotation. Temizer et al. [41, 42] presented two- and three-dimensional frictional contact treatment in isogeometric analysis with NURBS in the nite deformation regime. Howevere, it should be noted [38] that the IGA-C method is not a meshfree method since the isoparametric concept is adopted and meshes are employed either have a tensor product structure or are locally refined.

The novelty and intellectual contribution of this paper is using strong meshfree collocation method to model frictional contact problems as a first attempt. This study concentrates on Signorini-type problems by considering frictional contact constraint in strong form equation as a part of Neumann boundary condition. The key idea of the proposed method is directly discretize the strong form of governing partial differential equations based on Taylor polynomial expansion and the moving least square approach.

The main objective of this paper is to demonstrate the performance of the proposed method in solving one body

frictional contact engineering problems for which only a limited amount of literature in the public domain exist. The method does not require any kind of mesh thereby eliminating the need for numerical integration; i.e., point-wise computation. To demonstrate the capability of the proposed method, several benchmark problems in frictionless and frictional contact are provided. This paper is organized as follows: in Sect. 2 we provide a detailed derivation of the differential operators. The governing equations of linear elastic body, contact kinematics and constraint methodology, and penalty/regularization method are described in Sect. 3. Sect. 4 details the discretized equations in strong form for single-body contact, and the Newton–Raphson scheme to iteratively solve the equations. In Sect. 5, we present numerical examples and discuss the outcomes. Finally, conclusions are presented in Sect. 6 of the manuscript.

2 Problem description

We consider one body contact against a rigid obstacle for Signorini problem as shown in Fig. 1. The domain Ω is bounded by Γ i.e., $\bar{\Omega} = \Omega \cup \Gamma$. Assume that Γ is partitioned into Γ_u, Γ_t, Γ_c, which are Dirichlet and Neumann boundary conditions and contact constraints, respectively, i.e., $\Gamma = \Gamma_u \cup \Gamma_t \cup \Gamma_c$ with $\Gamma_u \cap \Gamma_t = \Gamma_u \cap \Gamma_c = \Gamma_c \cap \Gamma_t = \emptyset$.

We are interested in finding the displacement field $\mathbf{u}$ of the domain Ω such that the equilibrium is satisfied

$$\mathrm{div}\,\boldsymbol{\sigma} + \mathbf{b} = 0 \quad \text{in } \Omega, \tag{1}$$

where $\boldsymbol{\sigma}$ is the Cauchy stress tensor and $\mathbf{b}$ is a body force. For the constitutive assumption, we consider the linear elastic material, i.e.,

$$\boldsymbol{\sigma} = 2\mu\boldsymbol{\epsilon} + \lambda\mathrm{tr}(\boldsymbol{\epsilon})\mathbf{1}, \tag{2}$$
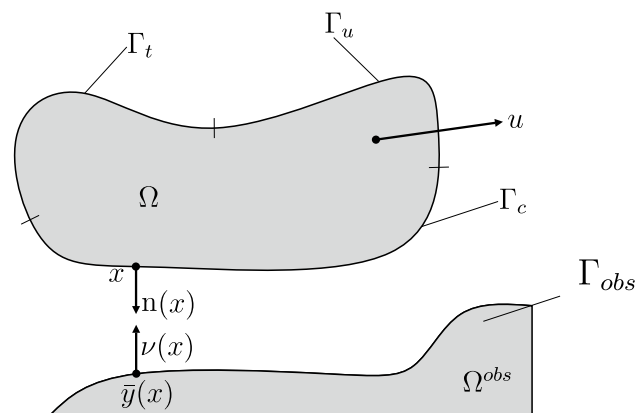
Fig. 1 Basic notation for the Signorini problem: one body contact against a rigid obstacle; here, $\boldsymbol{v}(\mathbf{x}) \approx -\mathbf{n}(\mathbf{x})$

where λ and μ are Lamé constants, $\mathbf{1}$ is the second-order identity tensor, and ϵ is the strain tensor defined by $\epsilon = (\nabla \mathbf{u} + (\nabla \mathbf{u})^\top)/2$. The Dirichlet and Neumann boundary conditions and contact constraints are given by

$$\begin{aligned} \mathbf{u} &= \bar{\mathbf{u}} & \text{on } \Gamma_u, \\ \boldsymbol{\sigma}\mathbf{n} &= \bar{\mathbf{t}} & \text{on } \Gamma_t, \\ \boldsymbol{\sigma}\mathbf{n} &= \mathbf{t}_c & \text{on } \Gamma_c, \end{aligned} \tag{3}$$

where $\mathbf{n}$ is the unit outward normal vector to domain Ω, $\bar{\mathbf{u}}$ is the prescribed displacement on Γ_u, $\bar{\mathbf{t}}$ is the prescribed traction on Γ_t, and $\mathbf{t}_c$ is the unknown contact traction on Γ_c. In plane strain, the Lamé constants are

$$\begin{aligned} \lambda &= \frac{\nu E}{(1 - 2\nu)(1 + \nu)} \\ \mu &= \frac{E}{2(1 + \nu)}, \end{aligned} \tag{4}$$

where E is Young's modulus, and ν is Poisson's ratio.

2.1 Contact kinematics

In this section, we introduce the contact constraints that govern the interaction between Ω and Ω^{obs}. Consider a point $\mathbf{x} \in \Gamma_c$ and assume for each such point $\mathbf{x}$, a corresponding point $\bar{\mathbf{y}}(\mathbf{x}) \in \Gamma_{\text{obs}}$ which is closest to $\mathbf{x}$ in Euclidean sense, i.e., $\bar{\mathbf{y}}(\mathbf{x}) = \arg\min||\mathbf{x} - \mathbf{y}||$. It should be noted that we have two surface normals, $\mathbf{n}(\mathbf{x})$ and $\boldsymbol{\nu}(\mathbf{x})$ which are associated with Γ_c and Γ^{obs}, respectively i.e., $\boldsymbol{\nu}(\mathbf{x}) \approx -\mathbf{n}(\mathbf{x})$ as shown in Fig. 1.

Given a displacement field $\mathbf{u} : \Gamma_c \to \mathbf{R}^2$, we define a gap function $g : \Gamma_c \to \mathbf{R}$ as follows. For all $\mathbf{x} \in \Gamma_c$,

$$g(\mathbf{x}) = g_0(\mathbf{x}) - \mathbf{u}(\mathbf{x}) \cdot \boldsymbol{\nu}(\mathbf{x}), \tag{5}$$

where $g_0(\mathbf{x}) = (\mathbf{x} - \bar{\mathbf{y}}(\mathbf{x}))\boldsymbol{\nu}(\mathbf{x})$ denotes the initial gap between two bodies or gap at zero displacement. To define the normal contact conditions, we will find it convenient to decompose the contact traction into normal and tangential components via

$$\mathbf{t}_c = \mathbf{t}_N - \mathbf{t}_T = t_N \boldsymbol{\nu} - t_T \boldsymbol{\tau}, \tag{6}$$

where $\boldsymbol{\nu}$ is the unit outward normal to Γ_c and $\boldsymbol{\tau}$ is the unit tangential vector defined as

$$\boldsymbol{\nu} = \mathbf{e}_3 \times \boldsymbol{\tau}, \tag{7}$$

where $\mathbf{e}_3$ is the unit basis vector pointing out of the paper.

The gap function g and contact pressure t_N are then related through the Kuhn–Tucker complementary conditions:

$$g(\mathbf{x}) \leq 0, \quad t_N(\mathbf{x}) \geq 0, \quad t_N g(\mathbf{x}) = 0. \tag{8}$$

Equation $(8)_2$ refers to the fact that if there is contact then the pressure is compressive. Equation $(8)_3$ is the requirement

that the pressure is nonzero only when contact occurs (i.e., $g = 0$). Further, when $g < 0$, this condition requires that t_N be zero, consistent with an out-of-contact condition.

2.2 Penalty algorithm

In this section, the contact constraints, i.e., both normal and frictional contact constraints are here regularized using the penalty method.

2.2.1 Definition of the normal contact constraints

A penalty regularization for the normal contact traction t_N is defined by the normal penalty parameter. We replace the contact pressure with the expression

$$t_N = \epsilon_N \langle g \rangle \tag{9}$$

where $\epsilon_N > 0$ is the normal penalty parameter and $\langle \bullet \rangle$ is the Macaulay bracket which represents the positive contribution of the operand, defined as

$$\langle g \rangle = \begin{cases} g & \text{if } g \geq 0, \\ 0 & \text{otherwise.} \end{cases} \tag{10}$$

The impenetrability condition is exactly satisfied as the penalty parameter $\epsilon_N \to \infty$. The normal contact constraint Eq. (9) is nonlinear and thus is linearized as

$$\triangle t_N = \triangle(\epsilon_N \langle g \rangle) = \epsilon_N \frac{\partial \langle g \rangle}{\partial g} \triangle g = H(g)\epsilon_N(-\delta\mathbf{u} \cdot \boldsymbol{\nu}), \tag{11}$$

where $H(g)$ is the Heaviside function and $\triangle(\cdot)$ denotes the directional derivative in the direction $\delta\mathbf{u}$. Here, we used the directional derivative of a function $f(\mathbf{u})$ in the direction $\delta\mathbf{u}$ defined as

$$\triangle f(\mathbf{u}) = \frac{\mathrm{d}}{\mathrm{d}\alpha}\bigg|_{\alpha=0} f(\mathbf{u} + \alpha\delta\mathbf{u}). \tag{12}$$

Notice that we use the small sliding approximation for the linearization, meaning that $\delta\boldsymbol{\nu}$ and $\delta\boldsymbol{\tau}$ are taken to be zero. In other words, the normal and tangent vectors are held constant during iterations, as is the contact point. Penalty parameters used for the numerical study are set within a range of two to three orders of magnitude of elastic modulus; within such a range, the numerical models robustly predict accurate solutions without suffering from severe dependencies on the adopted penalty parameters.

2.2.2 Definition of the frictional contact constraints

In this study, frictional contact constraint is obtained with the penalty approach. In the tangential direction, the regularized friction constraint can be written as

$$\phi := \|\mathbf{t}_\mathrm{T}\| - \mu t_\mathrm{N} \leq 0,$$

$$\mathbf{v}_\mathrm{T} - \dot{\zeta}\frac{\mathbf{t}_\mathrm{T}}{\|\mathbf{t}_\mathrm{T}\|} = \frac{1}{\epsilon_\mathrm{T}}\dot{\mathbf{t}}_\mathrm{T},$$

$$\dot{\zeta} \geq 0, \tag{13}$$

$$\dot{\zeta}\phi = 0$$

where $\epsilon_\mathrm{T} > 0$ is the tangential penalty parameter and μ is the coefficient of friction. Using backward Euler integrator to the penalty regularized spatial equations of evolution yields the following:

$$\phi := \|\mathbf{t}_\mathrm{T}\| - \mu t_\mathrm{N} \leq 0,$$

$$\mathbf{t}_\mathrm{T} = \epsilon_\mathrm{T}\left(\mathbf{u}_\mathrm{T} - \Delta\zeta\frac{\mathbf{t}_\mathrm{T}}{\|\mathbf{t}_\mathrm{T}\|}\right),$$

$$\Delta\zeta \geq 0, \tag{14}$$

$$\Delta\zeta\phi = 0.$$

A trial state/return mapping algorithm is employed to determine the Coulomb frictional traction. For implementation, the computational algorithm for Coulomb frictional traction is then given by:

1. The trial state is first computed by assuming no slip during the increment:

$$\mathbf{t}_T^{\mathrm{trial}} = \epsilon_\mathrm{T}\mathbf{u}_\mathrm{T},$$

$$\phi^{\mathrm{trial}} = \|\mathbf{t}_T^{\mathrm{trial}}\| - \mu t_\mathrm{N}. \tag{15}$$

   where $\mathbf{u}_\mathrm{T} = (\mathbf{1} - \mathbf{\nu}\otimes\mathbf{\nu})\mathbf{u}$ on Γ_c. Note that the normal contact pressure t_N is previously given by $t_N = \epsilon_\mathrm{N}\langle g\rangle$ in Eq. (9).

2. Check the status of stick or slip condition based on the pre-computed trial function ϕ^{trial}:

$$\mathbf{t}_\mathrm{T} = \begin{cases} \mathbf{t}_T^{\mathrm{trial}} & \text{if } \phi^{\mathrm{trial}} \leq 0 \text{ (stick)}, \\ \mu t_\mathrm{N}\frac{\mathbf{t}_T^{\mathrm{trial}}}{\|\mathbf{t}_\mathrm{T}^{\mathrm{trial}}\|} & \text{otherwise (slip)}. \end{cases} \tag{16}$$

3 Discretization of the strong form

The key idea of the proposed method is to use a standard Taylor series expansion with the moving least-squares approach to generate the shape functions and their derivatives to approximate the displacement field and its derivatives. The method uses the weight function to define compact support in order to generate a set of sparse discrete equations for the discretized system of equations. The strong forms are discretized using the precomputed derivative operators. In the following sections, we provide a brief description of the moving least-squares approximation based on

Taylor series expansion and discretization of the governing equations including contact constraints.

3.1 Meshfree collocation approximation

The details of approximate field variables and their derivatives can be found in Refs. [17–19], here, we provide the brief derivation of approximation. Using the Taylor series expansion with moving least-square approximation approach to higher-order derivatives of the shape functions. For convenience, we start by defining mathematical notation. Let $\mathbf{x} = (x_1, \ldots, x_n)$ be an n-dimensional real vector and $\boldsymbol{\alpha} = (\alpha_1, \ldots, \alpha_n)$ be an n-tuple of non-negative integers. The $\boldsymbol{\alpha}$th power of $\mathbf{x}$ is defined by

$$\mathbf{x}^{\boldsymbol{\alpha}} = x_1^{\alpha_1}x_2^{\alpha_2}\cdots x_n^{\alpha_n}. \tag{17}$$

We define the $\boldsymbol{\alpha}$th derivative of a smooth function $f(\mathbf{x})$ with respect to $\mathbf{x}$ as

$$D_{\mathbf{x}}^{\boldsymbol{\alpha}}f(\mathbf{x}) = \frac{\partial^{|\boldsymbol{\alpha}|}f(\mathbf{x})}{\partial x_1^{\alpha_1}\partial x_2^{\alpha_2}\cdots\partial x_n^{\alpha_n}}, \tag{18}$$

where $|\boldsymbol{\alpha}|$ is the sum of all components of $\boldsymbol{\alpha}$, i.e., $|\boldsymbol{\alpha}| \equiv \sum_{i=1}^n \alpha_i$.

Upon neglecting higher-order terms in a Taylor series, the mth-order polynomial for approximating a continuous function $u(\mathbf{x})$ at the local center $\bar{\mathbf{x}}$ can be expressed as

$$u(\mathbf{x};\bar{\mathbf{x}}) = \sum_{|\boldsymbol{\alpha}|\leq m}\frac{(\mathbf{x}-\bar{\mathbf{x}})^{\boldsymbol{\alpha}}}{\boldsymbol{\alpha}!}D_{\mathbf{x}}^{\boldsymbol{\alpha}}u(\bar{\mathbf{x}}) = \mathbf{p}_m^\top(\mathbf{x};\bar{\mathbf{x}})\mathbf{a}(\bar{\mathbf{x}}) \tag{19}$$

where $\boldsymbol{\alpha}!$ is the factorial of $\boldsymbol{\alpha}$, i.e., $\boldsymbol{\alpha}! = \alpha_1!\cdots\alpha_n!$. Note that as shown in Eq. (19), the Taylor polynomial can be decomposed into the polynomial vector $\mathbf{p}_m^\top(\mathbf{x};\bar{\mathbf{x}})$ and the derivative coefficient vector $\mathbf{a}(\bar{\mathbf{x}})$ computed at the local center. The polynomial vector takes the form

$$\mathbf{p}_m^\top(\mathbf{x};\bar{\mathbf{x}}) = \left[\frac{(\mathbf{x}-\bar{\mathbf{x}})^{\boldsymbol{\alpha}_1}}{\boldsymbol{\alpha}_1!}, \ldots, \frac{(\mathbf{x}-\bar{\mathbf{x}})^{\boldsymbol{\alpha}_L}}{\boldsymbol{\alpha}_L!}\right] \tag{20}$$

where $\boldsymbol{\alpha}_i$'s are an n-tuple of non-negative integers and $L = (n+m)!/n!m!$ is the number of the components of the polynomial vector $\mathbf{p}_m^\top$. Here, $(\mathbf{x}-\bar{\mathbf{x}})^{\boldsymbol{\alpha}_i}$ is the $\boldsymbol{\alpha}_i$th-power of $\mathbf{x}-\bar{\mathbf{x}}$ defined by $(\mathbf{x}-\bar{\mathbf{x}})^{\boldsymbol{\alpha}_i} = (x_1-\bar{x}_1)^{\alpha_{1i}}(x_2-\bar{x}_2)^{\alpha_{2i}}\cdots(x_n-\bar{x}_n)^{\alpha_{ni}}$. The derivative coefficient vector can be defined as

$$\mathbf{a}^\top(\bar{\mathbf{x}}) = \left[D_{\mathbf{x}}^{\boldsymbol{\alpha}_1}u(\bar{\mathbf{x}}), \ldots, D_{\mathbf{x}}^{\boldsymbol{\alpha}_L}u(\bar{\mathbf{x}})\right] \tag{21}$$

which includes all of the derivatives for $u(\bar{\mathbf{x}})$ at the local center up to the $\boldsymbol{\alpha}_L$th-order.

The collocation method uses the weight function $w\left(\frac{x-x_I}{\rho_I}\right)$ to define compact support which is non-zero over a neighborhood of x_I to generate set of sparse discrete equations for

the discretized system of equations. In contrast to most meshfree methods, the proposed method can use any function with a conical shape as the weight function. This is because no differentiability for the weight function is required in the formulation. As long as the function is non-negative and continuous, smoothness is not required. Thus, we use the non-differentiable functions

$$w_1\left(\frac{\mathbf{x}-\bar{\mathbf{x}}}{\rho_{\bar{\mathbf{x}}}}\right) = \left(1 - \left\|\frac{\mathbf{x}-\bar{\mathbf{x}}}{\rho_{\bar{\mathbf{x}}}}\right\|\right)^4 \tag{22}$$

and

$$w_2\left(\frac{\mathbf{x}-\bar{\mathbf{x}}}{\rho_{\bar{\mathbf{x}}}}\right) = \left(1 - \left\|\frac{\mathbf{x}-\bar{\mathbf{x}}}{\rho_{\bar{\mathbf{x}}}}\right\|^{1/2}\right)^2. \tag{23}$$

Bearing mind of the idea of moving least-square approximation, minimizing with respect to $\mathbf{a}(\bar{\mathbf{x}})$ the discrete form of the weighted, discrete L^2-norm given by

$$\mathbf{J} = \sum_{I=1}^{N} w\left(\frac{\mathbf{x}_I-\bar{\mathbf{x}}}{\rho_{\bar{\mathbf{x}}}}\right)[\mathbf{p}^\top(\mathbf{x}_I)\mathbf{a}(\bar{\mathbf{x}}) - u_I]^2 \tag{24}$$

yields

$$\mathbf{a}(\bar{\mathbf{x}}) = \mathbf{M}^{-1}(\bar{\mathbf{x}})\mathbf{B}(\bar{\mathbf{x}})\mathbf{u}^\top, \tag{25}$$

where the matrices $\mathbf{M}$ and $\mathbf{B}$ can be defined by

$$\mathbf{M}(\bar{\mathbf{x}}) = \sum_{I=1}^{N} w\left(\frac{\mathbf{x}_I-\bar{\mathbf{x}}}{\rho_{\bar{\mathbf{x}}}}\right)\mathbf{p}_m(\mathbf{x}_I;\bar{\mathbf{x}})\mathbf{p}_m^\top(\mathbf{x}_I;\bar{\mathbf{x}}), \tag{26}$$

$$\mathbf{B}(\bar{\mathbf{x}}) = w\left(\frac{\mathbf{x}_1-\bar{\mathbf{x}}}{\rho_{\bar{\mathbf{x}}}}\right)\mathbf{p}_m(\mathbf{x}_1;\bar{\mathbf{x}}), \dots, w\left(\frac{\mathbf{x}_N-\bar{\mathbf{x}}}{\rho_{\bar{\mathbf{x}}}}\right)\mathbf{p}_m(\mathbf{x}_N;\bar{\mathbf{x}}) \tag{27}$$

where the polynomial vector $\mathbf{p}_m(\mathbf{x}_I;\bar{\mathbf{x}})$ is defined in Eq. (20).

In Eq. (25), substituting $\mathbf{x}$ for $\bar{\mathbf{x}}$ and replacing $\mathbf{a}(\mathbf{x})$ with $\mathbf{D}_{\mathbf{x}}^\alpha u(\mathbf{x})$ yield

$$\mathbf{D}_{\mathbf{x}}^\alpha u(\mathbf{x}) = \sum_{I=1}^{N} \boldsymbol{\phi}_I^\alpha(\mathbf{x})u_I \tag{28}$$

where $\boldsymbol{\alpha} = (\alpha_1, \alpha_2)$ be a 2-tuple of non-negative integers. In matrix form, Eq. (28) can be expressed as

$$\begin{pmatrix} \mathbf{D}_{\mathbf{x}}^{\alpha_1}u(\mathbf{x}) \\ \mathbf{D}_{\mathbf{x}}^{\alpha_2}u(\mathbf{x}) \\ \vdots \\ \mathbf{D}_{\mathbf{x}}^{\alpha_L}u(\mathbf{x}) \end{pmatrix} = \begin{pmatrix} \boldsymbol{\phi}_1^{\alpha_1}(\mathbf{x}) & \boldsymbol{\phi}_2^{\alpha_1}(\mathbf{x}) & \cdots & \boldsymbol{\phi}_N^{\alpha_1}(\mathbf{x}) \\ \boldsymbol{\phi}_1^{\alpha_2}(\mathbf{x}) & \boldsymbol{\phi}_2^{\alpha_2}(\mathbf{x}) & \cdots & \boldsymbol{\phi}_N^{\alpha_2}(\mathbf{x}) \\ \vdots & \vdots & \ddots & \vdots \\ \boldsymbol{\phi}_1^{\alpha_L}(\mathbf{x}) & \boldsymbol{\phi}_2^{\alpha_L}(\mathbf{x}) & \cdots & \boldsymbol{\phi}_N^{\alpha_L}(\mathbf{x}) \end{pmatrix}\begin{pmatrix} u_1 \\ u_2 \\ \vdots \\ u_N \end{pmatrix} \tag{29}$$

where $\boldsymbol{\alpha}_i$'s are a 2-tuple of non-negative integers, e.g., $\boldsymbol{\alpha}_1 = (0,0)$, $\boldsymbol{\alpha}_2 = (1,0)$, $\boldsymbol{\alpha}_3 = (0,1)$, $\cdots$, $\boldsymbol{\alpha}_L = (0,m)$ for the mth order polynomial vector $\mathbf{p}_m$. Here, $\boldsymbol{\phi}_I^\alpha(\mathbf{x})$ is the $\boldsymbol{\alpha}$th derivative of the shape function at node I defined as

$$\boldsymbol{\phi}_I^\alpha(\mathbf{x}) = \mathbf{e}_\alpha^\top \mathbf{M}^{-1}(\mathbf{x})\mathbf{p}(\mathbf{x}_I;\mathbf{x})w\left(\frac{\mathbf{x}_I-\mathbf{x}}{\rho_{\mathbf{x}}}\right) \tag{30}$$

where $\mathbf{e}_\alpha^\top = [e_0, \cdots, e_m]$ with its component defined as

$$e_k = \begin{cases} 1 & \text{if } k = \alpha \\ 0 & \text{otherwise} \end{cases} \tag{31}$$

for $k = 0, \dots, m$.

3.2 Discretization for one-body frictional contact

In this section, we introduce the discretized strong-form governing equations with the proposed method, i.e., meshfree collocation method. For convenience, we define $Y = Y_i \cup Y_d \cup Y_t \cup Y_c$ where Y_i, Y_d, Y_t, and Y_c are sets of interior nodes, Dirichlet boundary nodes, Neumann boundary nodes, and nodes on contact surface Γ_c, respectively. Substituting Eq. (2) into Eq. (1) yields the governing equation

$$\mu\Delta\mathbf{u} + (\lambda + \mu)\nabla(div\,\mathbf{u}) + \mathbf{b} = 0 \quad \text{in } \Omega \tag{32}$$

which is enforced at the interior collocation points. In Cartesian components, Eq. (32) has the equivalent form

$$\mu u_{i,jj} + (\lambda + \mu)u_{j,ji} + b_i = 0 \quad \text{in } \Omega, \tag{33}$$

where $i,j = 1, 2$ in two dimensions and the repeated subscript follows the summation convention. For simplicity, we consider $\boldsymbol{\phi}_{IJ}^\alpha = \boldsymbol{\phi}_J^\alpha(\mathbf{x}_I)$ which is the value of the shape function at the collocation point $\mathbf{x}_I$. Substituting Eq. (28) into Eq. (33) yields the discrete form of equations which are given by

$$\sum_{J=1}^{N}\{[(\lambda + 2\mu)\boldsymbol{\phi}_{IJ}^{(2,0)} + \mu\boldsymbol{\phi}_{IJ}^{(0,2)}]u_{1I}$$
$$\quad + (\lambda + \mu)\boldsymbol{\phi}_{IJ}^{(1,1)}u_{2I}\} + b_1(\mathbf{x}_I) = 0,$$
$$\sum_{J=1}^{N}\{(\lambda + \mu)\boldsymbol{\phi}_{IJ}^{(1,1)}u_{1I} + [\mu\boldsymbol{\phi}_{IJ}^{(2,0)}$$
$$\quad + (\lambda + 2\mu)\boldsymbol{\phi}_{IJ}^{(0,2)}]u_{2I}\} + b_2(\mathbf{x}_I) = 0 \tag{34}$$

for the interior nodes $\mathbf{x}_J \in Y_i$.

The discrete form of the Dirichlet boundary condition can be obtained by substituting Eq. (28) into Eq. (3)$_1$ as

$$\sum_{J=1}^{N}\boldsymbol{\phi}_{IJ}^{(0,0)}u_{1I} - \bar{u}_{1I}(\mathbf{x}_J) = 0, \quad \sum_{J=1}^{N}\boldsymbol{\phi}_{IJ}^{(0,0)}u_{2I} - \bar{u}_{2I}(\mathbf{x}_J) = 0 \tag{35}$$

for $\mathbf{x}_J \in Y_d$.

Similarly, for the discretization of the Neumman boundary condition, i.e. Eq. (3)$_2$, substituting Eq. (2) into Eq. (3)$_2$ yields

$$2\mu\mathbf{n}\cdot\boldsymbol{\epsilon} + \lambda\mathbf{n}\cdot\mathbf{1}(\mathrm{div}\mathbf{u}) = \bar{\mathbf{t}} \quad \text{on } \Gamma_t \tag{36}$$

which, in Cartesian components, has the equivalent form

$$\mu(u_{i,j} + u_{j,i})n_j + \lambda\delta_{ij}n_j(u_{k,k}) = \bar{t}_i \quad \text{on } \Gamma_t \tag{37}$$

where δ_{ij} is the Kronecker delta. For the discretization of Eq. (37) with the PDM, substituting Eq. (28) into Eq. (37) results in

$$\sum_{J=1}^{N}\{[(\lambda + 2\mu)\boldsymbol{\phi}_{IJ}^{(1,0)}n_1 + \mu\boldsymbol{\phi}_{IJ}^{(0,1)}n_2]u_{1I} + [\lambda\boldsymbol{\phi}_{IJ}^{(0,1)}n_1$$
$$+ \mu\boldsymbol{\phi}_{IJ}^{(1,0)}n_2]u_{2I}\} - t_1(\mathbf{x}_I) = 0,$$
$$\sum_{J=1}^{N}\{[\mu\boldsymbol{\phi}_{IJ}^{(0,1)}n_1 + \lambda\boldsymbol{\phi}_{IJ}^{(1,0)}n_2]u_{1I} + [(\lambda + 2\mu)\boldsymbol{\phi}_{IJ}^{(0,1)}n_2$$
$$+ \mu\boldsymbol{\phi}_{IJ}^{(1,0)}n_1]u_{2I}\} - t_2(\mathbf{x}_I) = 0 \tag{38}$$

$$\sum_{J=1}^{N}\{[(\lambda + 2\mu)\boldsymbol{\phi}_{IJ}^{(1,0)}n_1 + \mu\boldsymbol{\phi}_{IJ}^{(0,1)}n_2]\delta u_{1I} + [\lambda\boldsymbol{\phi}_{IJ}^{(0,1)}n_1$$
$$+ \mu\boldsymbol{\phi}_{IJ}^{(1,0)}n_2]\delta u_{2I}\} + \epsilon_{\mathrm{N}}H(g(\mathbf{x}_J))(\delta\mathbf{u}(\mathbf{x}_J)\cdot\boldsymbol{\nu})\nu_1$$
$$+ \epsilon_{\mathrm{T}}H(g(\mathbf{x}_J))(\delta\mathbf{u}\cdot\boldsymbol{\tau})\tau_1 = 0,$$
$$\sum_{J=1}^{N}\{[\mu\boldsymbol{\phi}_{IJ}^{(0,1)}n_1 + \lambda\boldsymbol{\phi}_{IJ}^{(1,0)}n_2]\delta u_{1I} + [(\lambda + 2\mu)\boldsymbol{\phi}_{IJ}^{(0,1)}n_2$$
$$+ \mu\boldsymbol{\phi}_{IJ}^{(1,0)}n_1]\delta u_{2I}\} + \epsilon_{\mathrm{N}}H(g(\mathbf{x}_J))(\delta\mathbf{u}(\mathbf{x}_J)\cdot\boldsymbol{\nu})\nu_2$$
$$+ \epsilon_{\mathrm{T}}H(g(\mathbf{x}_J))(\delta\mathbf{u}\cdot\boldsymbol{\tau})\tau_2 = 0 \tag{43}$$

for $\mathbf{x}_J \in Y_c$ in the case of stick region. For the slip case, equation is given by

$$\mu(u_{i,j} + u_{j,i})n_j + \lambda\delta_{ij}n_j(u_{k,k}) - \epsilon_{\mathrm{N}}\langle g(\mathbf{x}_J)\rangle\nu_i + \mu t_{\mathrm{N}}\mathrm{sign}(t_{\mathrm{T}}^{\mathrm{trial}})\tau_i = 0. \tag{44}$$

For the discretization of Eq. (44) with the PDM, substituting Eq. (28) into Eq. (44) results in

$$\sum_{J=1}^{N}\{[(\lambda + 2\mu)\boldsymbol{\phi}_{IJ}^{(1,0)}n_1 + \mu\boldsymbol{\phi}_{IJ}^{(0,1)}n_2]\delta u_{1I} + [\lambda\boldsymbol{\phi}_{IJ}^{(0,1)}n_1 + \mu\boldsymbol{\phi}_{IJ}^{(1,0)}n_2]\delta u_{2I}\}$$
$$+ \epsilon_{\mathrm{N}}H(g(\mathbf{x}_J))(\delta\mathbf{u}(\mathbf{x}_J)\cdot\boldsymbol{\nu})\nu_1 - \mu\epsilon_{\mathrm{N}}H(g(\mathbf{x}_J))(\delta\mathbf{u}(\mathbf{x}_J)\cdot\boldsymbol{\nu})\mathrm{sign}(\mathbf{u}\cdot\boldsymbol{\tau})\tau_1 = 0,$$
$$- H(g(\mathbf{x}_J))\epsilon_{\mathrm{N}}(\delta\mathbf{u}(\mathbf{x}_J)\cdot\mathbf{n})n_2\sum_{J=1}^{N}\{[\mu\boldsymbol{\phi}_{IJ}^{(0,1)}n_1 + \lambda\boldsymbol{\phi}_{IJ}^{(1,0)}n_2]\delta u_{1I} + [(\lambda + 2\mu)\boldsymbol{\phi}_{IJ}^{(0,1)}n_2 + \mu\boldsymbol{\phi}_{IJ}^{(1,0)}n_1]\delta u_{2I}\}$$
$$+ H(g(\mathbf{x}_J))\epsilon_{\mathrm{N}}(\delta\mathbf{u}(\mathbf{x}_J)\cdot\boldsymbol{\nu})\nu_2 - \mu\epsilon_{\mathrm{N}}H(g(\mathbf{x}_J))(\delta\mathbf{u}(\mathbf{x}_J)\cdot\boldsymbol{\nu})\mathrm{sign}(\mathbf{u}\cdot\boldsymbol{\tau})\tau_2 = 0 \tag{45}$$

for $\mathbf{x}_J \in Y_t$.

Now, we replace $\mathbf{t}^c$ ($\mathbf{t}^c = \mathbf{t}_{\mathrm{N}} - \mathbf{t}_{\mathrm{T}}$) in Eq. (3)$_3$ in order to model normal and tangential tractions, i.e.,

$$2\mu\mathbf{n}\cdot\boldsymbol{\epsilon} + \lambda\mathbf{n}\cdot\mathbf{1}(\mathrm{div}\mathbf{u}) - \mathbf{t}^c = 0 \quad \text{on } \Gamma_c \tag{39}$$

which, in Cartesian components, has the equivalent form

$$\mu(u_{i,j} + u_{j,i})n_j + \lambda\delta_{ij}n_j(u_{k,k}) - t_{\mathrm{N}}\nu_i + t_{\mathrm{T}}\tau_i = 0 \quad \text{on } \Gamma_c \tag{40}$$

where δ_{ij} is the Kronecker delta. Applying Eq. (9) to t_{N} and Eq. (15) and Eq. (16) to t_{T} yields

$$\mu(u_{i,j} + u_{j,i})n_j + \lambda\delta_{ij}n_j(u_{k,k}) - \epsilon_{\mathrm{N}}\langle g(\mathbf{x}_J)\rangle n_i + t_{\mathrm{T}}^{\mathrm{trial}}\tau_i = 0. \tag{41}$$

For the stick case,

$$\mu(u_{i,j} + u_{j,i})n_j + \lambda\delta_{ij}n_j(u_{k,k}) - \epsilon_{\mathrm{N}}\langle g(\mathbf{x}_J)\rangle\nu_i + H(g(\mathbf{x}_J))t_{\mathrm{T}}^{\mathrm{trial}}\tau_i = 0. \tag{42}$$

For the discretization of Eq. (42) with the PDM, substituting Eq. (28) into Eq. (42) results in

for $\mathbf{x}_J \in Y_c$ in the case of slip region.

To this end, the nonlinear system of equation can be written as

$$\mathbf{R}(\mathbf{u}) = \mathcal{L}(\mathbf{u}) - \mathcal{F}(u) = 0 \tag{46}$$

where $\mathbf{R}$ is residual that is considered to be a nonlinear function of the solution vector $\mathbf{u}$. A Newton–Raphson scheme apply to Eq. (46) in iteration j by

$$\mathbf{R}(\mathbf{u}_j) + \frac{\partial\mathbf{R}}{\partial\mathbf{u}}\bigg|_j \delta\mathbf{u} = \mathbf{0}, \tag{47}$$

where $\frac{\partial\mathbf{R}}{\partial\mathbf{u}}$ as the tangent stiffness matrix $\mathbf{K}$, and followed by the update

$$\mathbf{u}_{j+1} = \mathbf{u}_j + \delta\mathbf{u}, \tag{48}$$

where the subscripts $j + 1$ and j correspond to the current and previous Newton–Raphson iteration of the current load step n, respectively.

Convergence criterion is defined by the ratio of the solution increment $\delta\mathbf{u}_j$ within a current iteration $j + 1$ relative to

the last converged load step n. Convergence is assumed to occur when their relative ratios fall below a user specified tolerance TOL $= 10^{-12}$. For instance, the convergence criterion in terms of the solution increment is given by

$$\frac{||\delta\mathbf{u}||}{||\mathbf{u}_{j+1} - \mathbf{u}_n||} < \text{TOL} \tag{49}$$

During the Newton–Raphson solution procedure, at each current iteration $j + 1$, we follow subsequently described procedures:

1. Compute the residual $\mathbf{R}(\mathbf{u})$ and tangent $\mathbf{K}(\mathbf{u})$ using the solution $\mathbf{u}$ from the last converged step j.
2. Use Eq. (47) to solve for $\delta\mathbf{u}$,
3. Use Eq. (48) to update $\mathbf{u}$, and
4. Repeat steps 1–3 above until convergence values as defined by Eq. (49) are satisfied.

The stiffness matrix $\mathbf{K}$ can be obtained by

$$\mathbf{K} = \begin{bmatrix} K^{int} & 0 & 0 & 0 \\ 0 & K^D & 0 & 0 \\ 0 & 0 & K^N & 0 \\ 0 & 0 & 0 & K^c \end{bmatrix}. \tag{50}$$

The components of stiffness matrix (i.e., K^{int}, K^D, K^N, and K^c) and components of force vectors ($\mathbf{f}^c_{\text{slip}}$ and $\mathbf{f}^c_{stick}$) are defined in Appendix 1.

4 Numerical study

In this section, the performance of the proposed method for practical applications is tested for frictional contact problems with various contact geometric shapes and loading conditions. The method is applied to three types of problems consisting of an elastic slab on a rigid plate under both vertical and horizontal compressive loads, a rectangular block contacting with a circular inclusion, and an elastic foundation contacting with a rigid pile. To check accuracy of the method, numerical results are compared with the results of ABAQUS [43] using the plane strain elements (CPE4R). We considered the penalty method for contact enforcement in ABAQUS/Standard, and the other parameters e.g. material properties, frictional coefficient, and loading conditions are same as the collocation method.

Notice that the upper and lower bounds of the compact support sizes ensure the invertibility of the moment matrix $\mathbf{M}$ which is described in Eq. (26). In this study, spatially varying continuous compact support function is constructed to evaluate the compact support size at each collocation point. The dilation parameter $\rho_{\bar{\mathbf{x}}}$ is chosen based
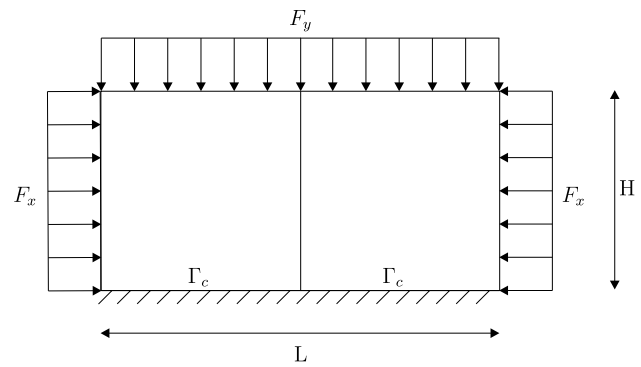
Fig. 2 Contact between an axially compressed elastic slab and a rigid plate
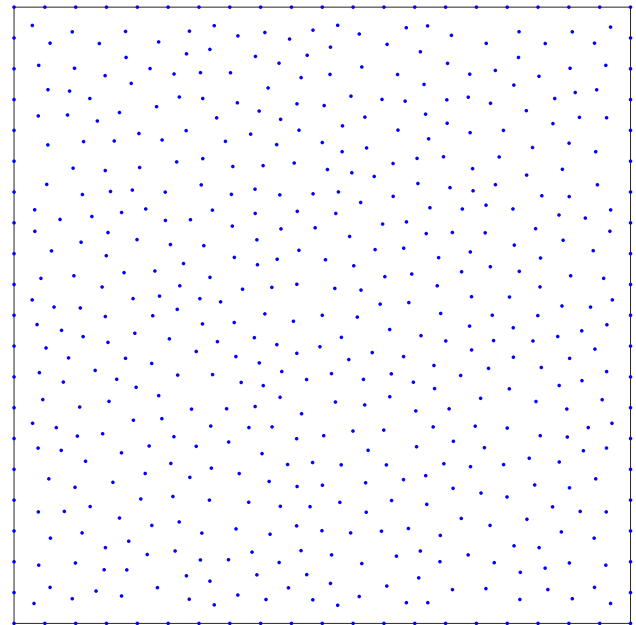

Fig. 3 A half slab with non-uniformly distributed 558 collocation points. The contact surface Γ_c with a rigid plate is located on the bottom

on a pseudo-collocation point counting approach [28] that can measure the spatial variation of the collocation density.

4.1 An elastic slab on a flat rigid plate

To validate the frictional contact algorithm [44], we model contact of a symmetrically loaded elastic slab set on top of a rigid plate obstacle. As shown in Fig. 2, the slab with the ratio of length to height of $L/H = 2$ is axially loaded in both x- and y-directions, i.e., $F_y = 5$ daN/mm^2 and $F_x = 2F_y$. Consistent with [44], we take the material properties of $E = 13000$ daN/mm^2 and $\nu = 0.2$, and the frictional coefficient $\mu = 1.0$. The penalty parameters are chosen to be

Fig. 4 Distribution of **a** the displacement u_{xx} and **b** the shear stress σ_{xy} for an elastic solid on a rigid plate

(a)   (b)

(a)   (b)
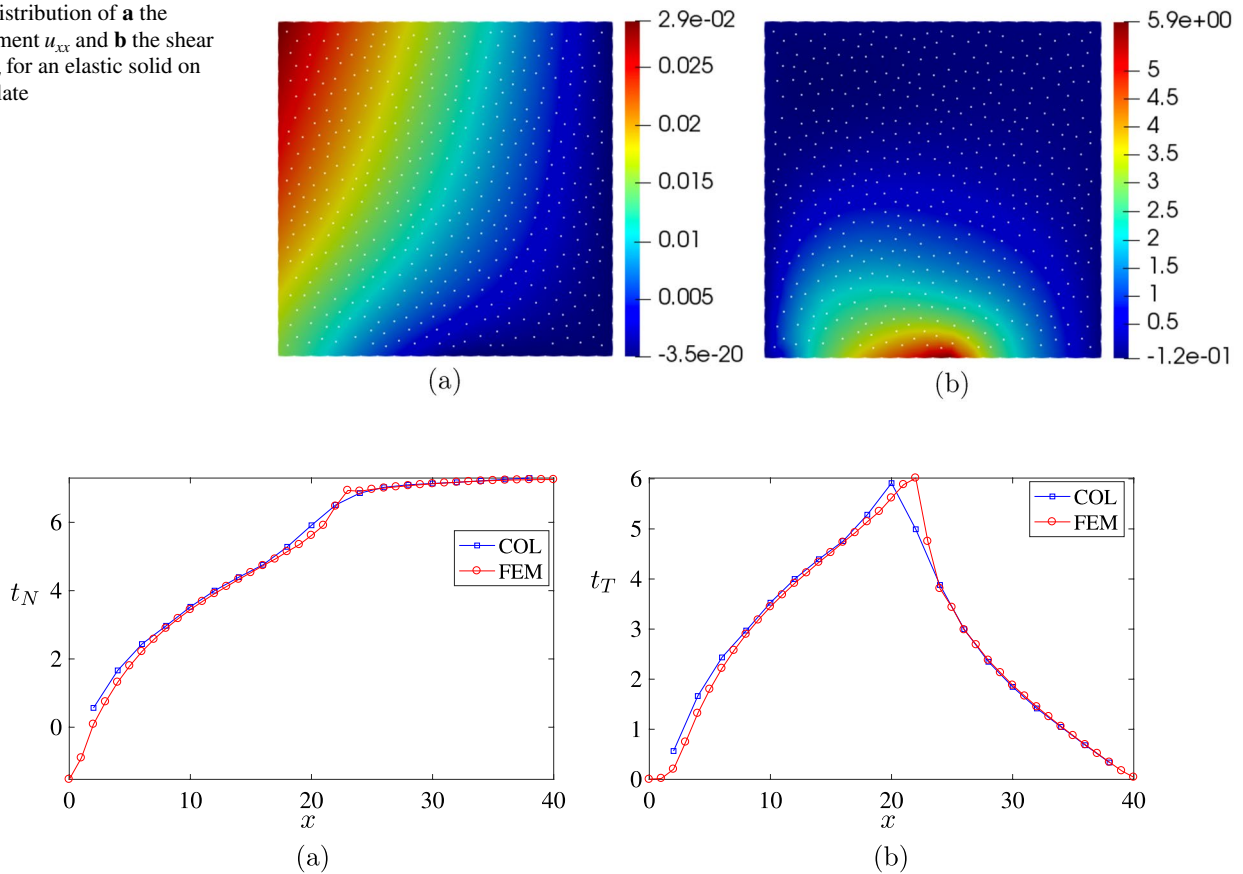
Fig. 5 Contact tractions by the proposed collocation (COL) method and the FEM using ABAQUS: **a** normal traction t_N and **b** tangential traction t_T

$\epsilon_N = \epsilon_T = 10^5$. Notice that, due to the symmetry, only a left half slab in Fig. 2 is modeled as the computational domain. In Fig. 3, we display the model of the non-uniformly distributed 558 collocation points on the half slab that was used for this study. The contact surface Γ_c with a rigid obstacle is located on the bottom of the half slab and the symmetric boundary condition is applied on its right side.

Displacement field u_{xx} and shear stress σ_{xy} distributions are presented in Fig. 4. As expected, on the contact surface at the bottom, the discontinuity of the displacement is clearly visible on the left zone, indicating slip along the contact surface. The distribution of the shear stress is qualitatively close to the result of Fig. 11 in Renaud and Feng [44]. To verify accuracy of the method, contact tractions obtained from the strong form collocation (COL) method are compared with the results from the FEM using ABAQUS in Fig. 5. Normal and tangential traction profiles are similar to each other. However, as shown in Fig. 5b certain differences exist around stick/slip transition area between the two methods. Quantifying the cause is an area of active research, the results of which will be published in future works.
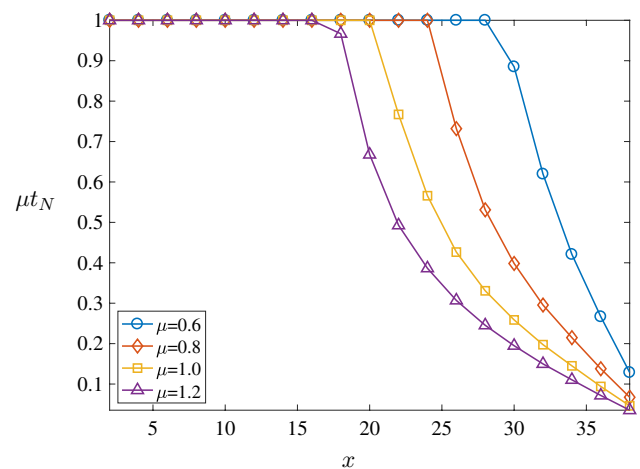
Fig. 6 The stick-slip response of the elastic slab on a rigid plate

Figure 6 provides stick-slip response behavior on the contact surface for various frictional coefficient values. To study the effect of the frictional coefficient on the contact surface,
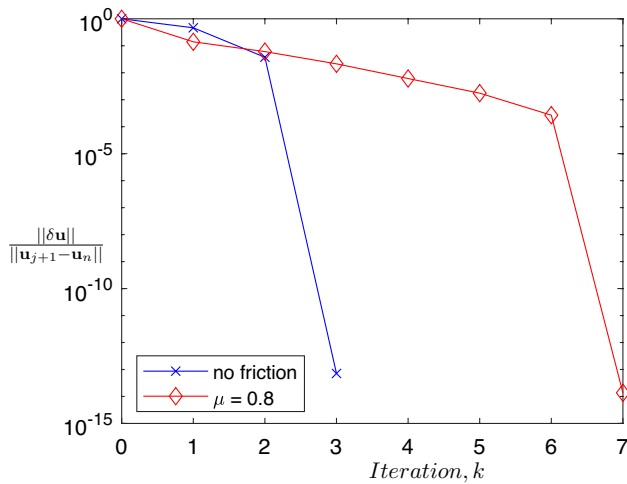
Fig. 7 Convergence behavior during the first load step for frictional and frictionless contact

we employ the ratio of the tangential traction to the normal traction, i.e., $t_T/\mu t_N$, indicating that, from the slip condition (16), the contact region is slip if $t_T/\mu t_N = 1$, otherwise it is stick. Growth of the slip region and corresponding reduction of the stick region are observed for decreasing μ. These results show the proposed collocation algorithm is able to accurately reproduce the stick-slip response behavior of one-body frictional contact on the flat contact surface.

The convergence plot for the frictional (i.e., $\mu = 0.8$) and frictionless (i.e. $\mu = 0$) contact during the first load step is presented in Fig. 7. For most iterations, a subset of contact nodes undergoes a transition from stick to slip condition where the trial state t_T^{trial} as defined in Eq. (3.15) continues to evolve resulting in linear convergence rate. For a contact node, convergence of t_T^{trial} to a value results in a significant reduction in the residual for the node implying equilibrium between contact and interior forces at that node.

4.2 An elastic block with a rigid cylinder inclusion

In this section, the capability of the proposed collocation method is tested for an elastic block with a rigid cylinder inclusion as shown in Fig. 8. This example is a Signorini-type problem consisting of a deformable body around a rigid circular cylinder is stretched by a uniform traction [45]. We choose the block with $L = 16$ and $H = 12$. The radii of the hole and the rigid cylinder are respectively taken as $R = 2.0$ and $r = 1.9$ as shown in the figure. The block is uniformly stretched to the left by applying the prescribed traction, $t_x = 25$, resulting in contact with a rigid cylinder. Due to symmetry, we only consider an upper half of the block as the computational domain as shown in Fig. 9a. We assume the material properties of $E = 10^3$ and $\nu = 0.3$. For normal contact constraint, the penalty parameter is taken to be $\epsilon_N = 10^5$. Fig. 9b shows the model of the non-uniformly distributed collocation points that are locally refined in the vicinity of the contact region.

Horizontal displacement, u_{xx}, and the stress, σ_{xx}, distributions are presented Fig. 10a, b, respectively. The plots show the kinematic constraint imparted on the displacement field of the elastic body, $u_{xx} = 0$, due to the rigid cylinder along

Fig. 8 Problem description for an elastic block contact with a rigid cylinder inclusion
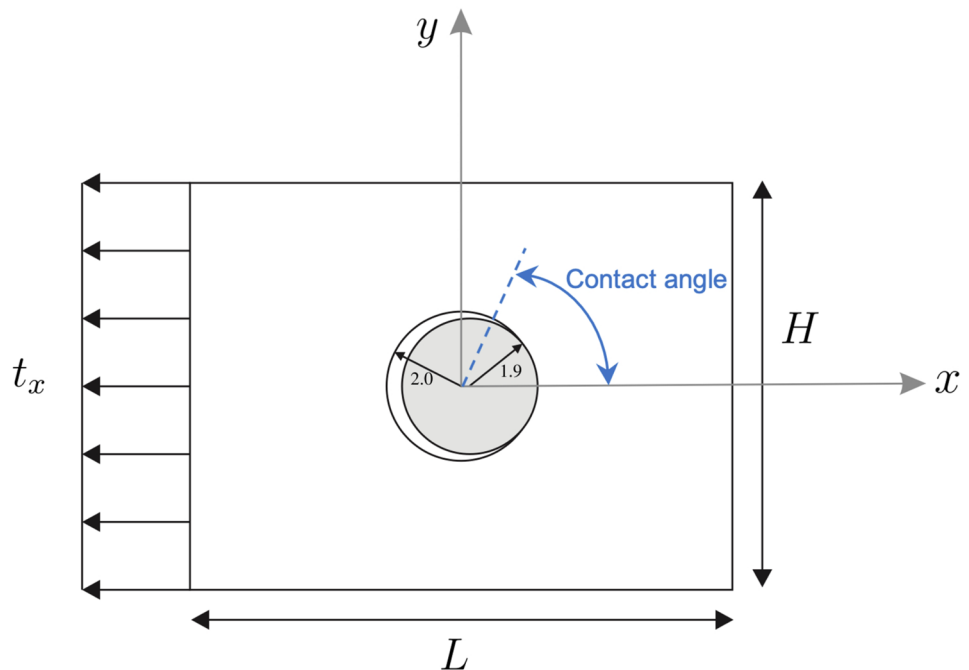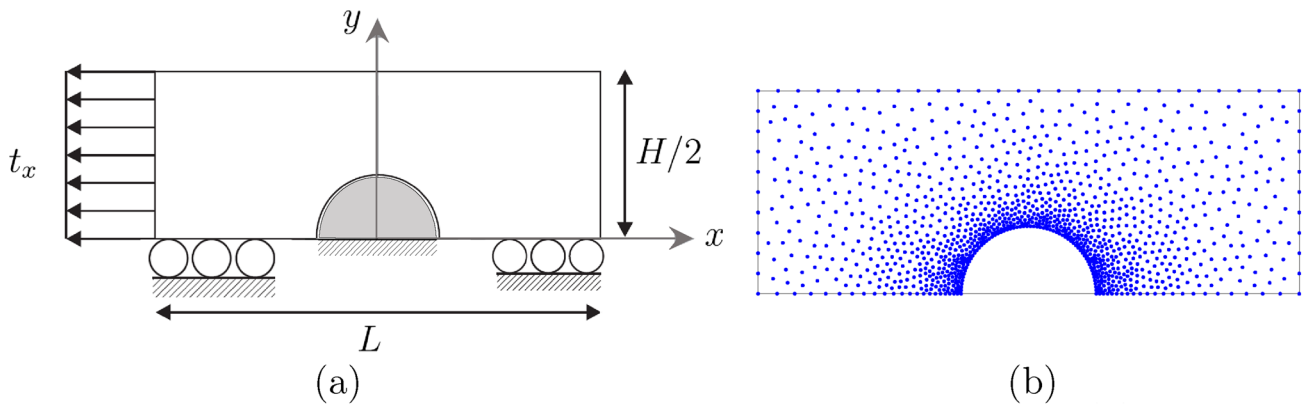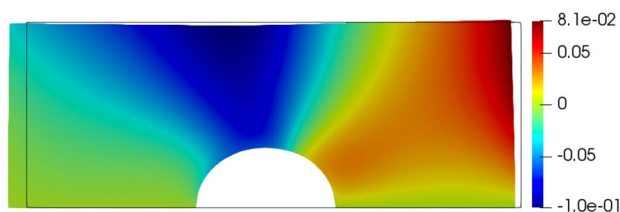
Fig. 9 **a** An upper half region of the block due to symmetry and **b** non-uniformly distributed 1142 collocation points refined near the cylindrical contact region
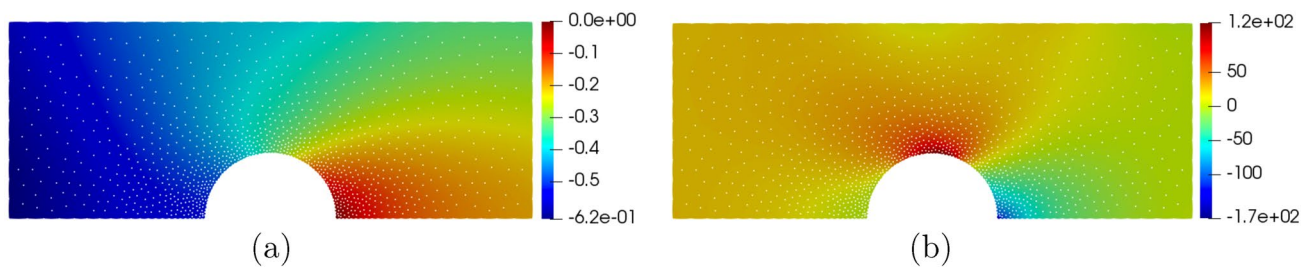
Fig. 10 Contour plots of **a** the displacement u_{xx} and **b** the stress σ_{xx} for an elastic block with a rigid cylinder frictionless contact

the region of contact. A corresponding (relatively high) stress concentration is observed in the same vicinity. In Figure 11, we also display a deformed body of the elastic block around a rigid cylinder by plotting the displacement u_{yy}.

A comparison of normal traction values, t_N, between collocation and FEM models generated with ABAQUS are provided in Fig. 12. where results from both simulations are qualitatively in good agreement without significant deviation. The plot clearly shows the occurrence of the contact region in which the normal traction is nonzero due to the stretched uniform normal traction to the left. Moreover, the effect of Young's modulus (E) on the angle of the contact area for a rigid cylinder is summarized in Table 1.

The predicted contact angle for, $E = 10^3$, is 68.6° is in good agreement with the value presented in Kikuchi and Oden study [45] of 66°. The result shows that, as E is increased, the contact angle becomes smaller, indicating the decrease of the contact region due to smaller deformation of the block.

Next, we consider the frictional contact with the frictional coefficient $\mu = 0.3$. The penalty parameters used for this study are $\epsilon_N = \epsilon_T = 10^4$. The same settings for other parameters with the frictionless contact are chosen. The normal and tangential tractions in the vicinity of the contact area are compared with the results from the FEM using ABAQUS in Fig. 13. Both tractions from the proposed collocation method are qualitatively close to those of the FEM.

Fig. 11 Initial and deformed shape of an elastic block due to frictionless contact with a rigid cylinder

Table 1 Effect of the contact angle on various values of Young's modulus E for the frictionless rigid cylinder contact

Young's modulus (E)	Contact angle (°)
1×10^3	68.6
1.5×10^3	62.8
2.0×10^3	57.1
2.5×10^3	51.4
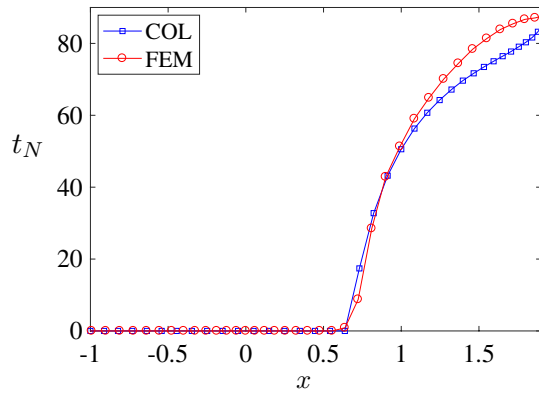
Fig. 12 Contact normal traction t_N by the proposed collocation method and the FEM using ABAQUS for an elastic block with a rigid cylinder frictionless contact

4.3 Hertzian contact problem

In this study, we examine error behavior of our method based on the local refinement of the collocation points near the contact region. For quantitative study of the error, two types of error norms are considered. One is to measure local error at the contact surface using normal traction t_N, and the other is for global error over the entire domain using the displacement **u**. Notice that the error behavior is investigated using the numerical reference solutions obtained from the most refined collocation points over the whole domain Ω.

In doing so, we define the displacement error norms in the discrete L^2 and L^∞ as

$$\left\| e_{\mathbf{u}} \right\|_2 = \frac{\left\| \mathbf{u}_i^h - \mathbf{u}_i^{\mathrm{ref}} \right\|}{\left\| \mathbf{u}_i^{\mathrm{ref}} \right\|}, \quad \left\| e_{\mathbf{u}} \right\|_\infty = \frac{\max_i \left\| \mathbf{u}_i^h - \mathbf{u}_i^{\mathrm{ref}} \right\|}{\max_i \left\| \mathbf{u}_i^{\mathrm{ref}} \right\|}, \quad (51)$$

where $\mathbf{u}^h \in \Omega$ is the approximation of the displacement **u** and $\mathbf{u}^{\mathrm{ref}}$ is the numerical reference solution. For the local error measurement on the contact surface, we define the contact pressure error norms in the discrete L^2 and L^∞ as

$$\left\| e_{\mathbf{t}_N} \right\|_2 = \frac{\left\| (\mathbf{t}_N)_i^h - (\mathbf{t}_N)_i^{\mathrm{ref}} \right\|}{\left\| (\mathbf{t}_N)_i^{\mathrm{ref}} \right\|}, \quad \left\| e_{\mathbf{t}_N} \right\|_\infty = \frac{\max_i \left\| (\mathbf{t}_N)_i^h - (\mathbf{t}_N)_i^{\mathrm{ref}} \right\|}{\max_i \left\| (\mathbf{t}_N)_i^{\mathrm{ref}} \right\|}, \quad (52)$$

where $\mathbf{t}_N^h \in \Gamma_c$ is the approximation of the contact pressure and $\mathbf{t}_N^{\mathrm{ref}}$ is the analytical reference solution of the contact pressure on the local contact region Γ_c.

The problem we used for this study is a cylindrical frictionless Hertzian contact problem on a rigid obstacle. The Hertzian contact is schematically described in Fig. 14. The cylinder is modelled as an isotropic linear elastic material with $E = 200$ and $\nu = 0,3$ with the radius of a cylinder $R = 10$. We take the penalty parameter of $\epsilon_N = 10^6$. A half-cylinder is pressed by a distributed pressure $t_y = -1.0$, resulting in normal traction at the contact surface.

To study error behavior of the method, we employ four different types of non-uniformly distributed collocation points with local refinement in the vicinity of the contact surface as shown in Fig. 15. In Tables 2 and 3, we summarize the displacement and contact pressure error behavior in both L^2- and L^∞-norms. Averaged wall-clock time as well as averaged number of Newton–Raphson iterations at each load step are also presented in Table 2 to further provide insights to the computational algorithm's performance characteristics; they are the mean of all values recorded at the end of each load step with clock values normalized to the coarsest discretization. We compute the average nodal spacing h_{avg} for the measurement of the resolution. Decreasing h_{avg} means the resolution becomes finer, and otherwise coarser. The results show the tendency of the slight reduction of both local and global errors with increasing the resolution. Figure 16 shows the plots of the contact normal tractions at the contact surface for four different randomly distributed collocation points. With increasing the local refinement, the numerical solution approaches to the analytical solution, indicating the efficiency of the proposed method for adaptivity. The spatial convergence rate [46] for Hertzian contact problem can be found in the authors' previous work.

Fig. 13 Comparison of the proposed collocation (COL) method with the FEM using ABAQUS: **a** normal traction t_N and **b** tangential traction t_T


(a)

(b)
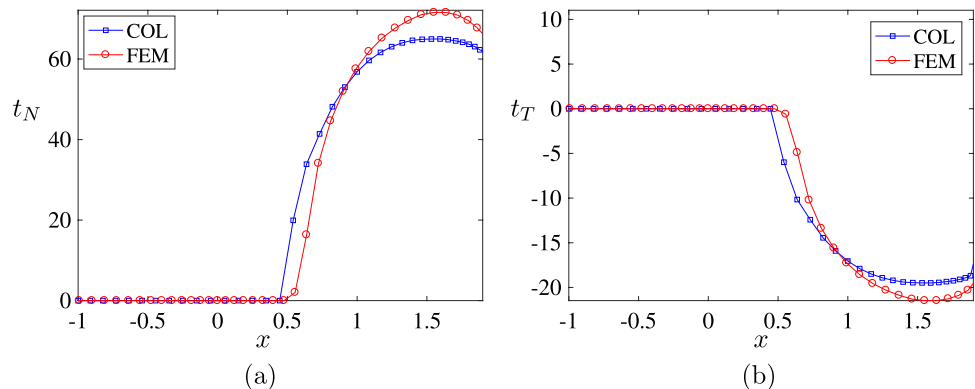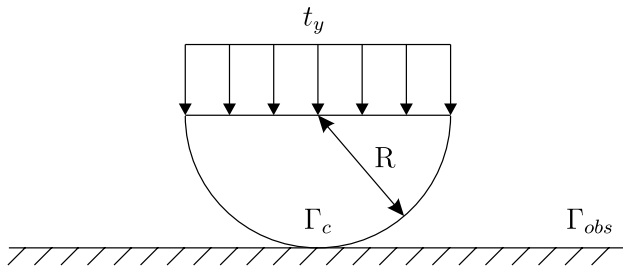
Fig. 14 Problem description of Hertzian frictionless contact: a half cylinder subjected to the uniform distributed pressure t_y

However, the in-depth comparison against the FEM remains as a future work.

4.4 Frictional contact between a rigid pile and an elastic foundation

In this section, we apply our method to a straight axially loaded pile embedded in a homogeneous elastic foundation. The problem is graphically described in in Fig. 17. This study focuses on frictional contact between a rigid pile with a radius of $R = 0.5$ at the end of the pile and an elastic foundation with length $L = 9.0$ and height $H = 8.0$. Notice that the range of the contact surface in the vertical direction, i.e., $y \in \Gamma_c$, is defined as $H/2 \leq y \leq H$, (i.e., $4 \leq y \leq 8$ with
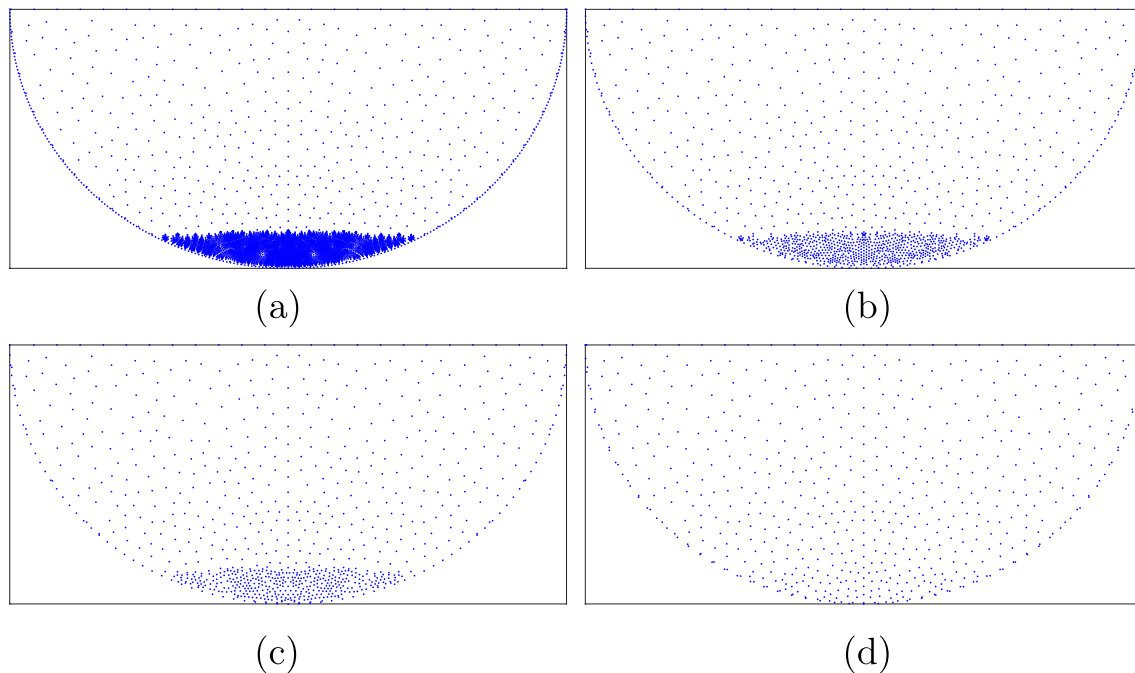
Fig. 15 **a** Non-uniformly distributed 6520 collocation points with local refinement ($h_{avg} = 0.08$), **b** non-uniformly distributed 1254 collocation points with local refinement ($h_{avg} = 0.15$), **c** non-uniformly distributed 902 collocation points with local refinement ($h_{avg} = 0.27$), and **d** non-uniformly distributed 614 collocation points with local refinement ($h_{avg} = 0.51$)

**Table 2** Displacement errors in the discrete L^2- and L^∞-norms for the Hertzian contact

h_{avg}	Total # of col. pts	# of col. pts on Γ_c	$\|e_\mathbf{u}\|_2$	$\|e_\mathbf{u}\|_\infty$	Wall-clock time[a]	NR iterations[a]
0.08	6520	31	–	–	1	2.8
0.15	1254	15	0.92e−2	1.4e−2	1.6e−2	2.2
0.27	902	11	1.4e−2	2.1e−2	8.5e−3	2.2
0.51	614	7	2.2e−2	8.1e−2	4.6e−3	2.2

Wall-clock time and number of Newton–Raphson iterations are averaged values per load step; wall-clock time is further normalized to the coarsest discretization
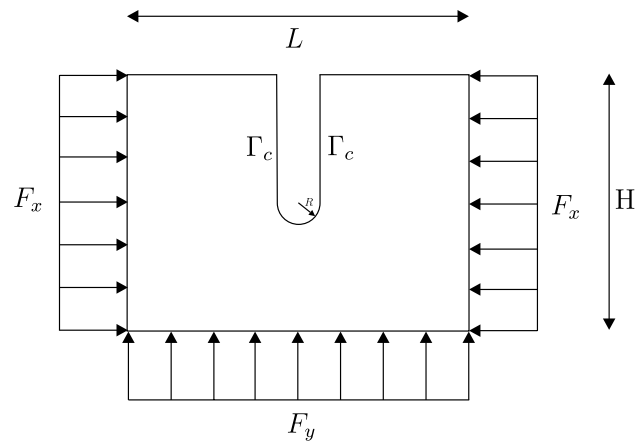
[a]Averaged values per load step

Table 3 Contact pressure errors in the discrete L^2- and L^∞-norms for the Hertzian contact problem

h_{avg}	Total # of col. pts	# of col. pts on Γ_c	$\left\| e_{\mathbf{t}_N} \right\|_2$	$\left\| e_{\mathbf{t}_N} \right\|_\infty$
0.08	6520	31	2.8e−2	5.2e−2
0.15	1254	15	4.9e−2	6.9e−2
0.27	902	11	4.4e−2	5.4e−2
0.51	614	7	8.5e−2	8.7e−2
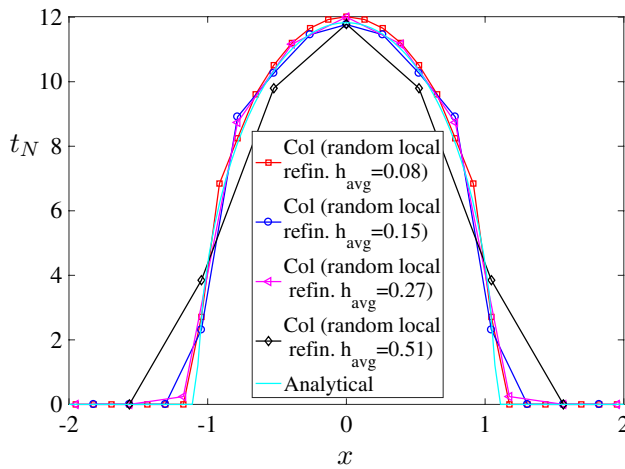
Fig. 16 Comparisons of the normal contact traction t_N at Γ_c with four different sets of randomly distributed collocation points for Hertzian contact


Fig. 17 Problem description of contact between rigid pile and elastic foundation
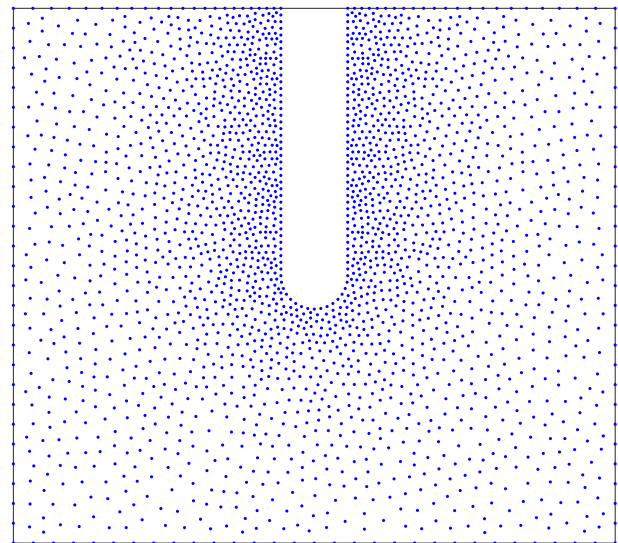
Fig. 18 Non-uniformly distributed 2492 collocation points refined near the contact region

$H = 8.0$). The prescribed tractions of $F_x = 4$ and $F_y = 2$ are applied to both axial directions as shown in the figure. As a result, we expect that the horizontal deformation is more significant than the vertical one. We use $E = 10^3$ and $\nu = 0.3$ as the material properties of the elastic foundation. The frictional contact is modelled by choosing the frictional coefficient $\mu = 0.8$ and the penalty parameters of $\epsilon_N = \epsilon_T = 10^6$. In Fig. 18, we display the collocation point model used for this study. Motivated by the study in the previous examples, non-uniformly distributed collocation points are locally refined in the vicinity of the contact region between a rigid plate and the foundation for efficient simulation.

Figures 19 and 20 show the distributions of the displacement and stress fields in both x- and y- directions, respectively, on the elastic foundation. The displacement distributions along the contact surface Γ_c, including prevention of interpenetration between the foundation and the rigid pile, are qualitatively reasonable. The displacement in the y-direction is relatively smaller than one in the x-direction because

of the applied traction condition, i.e., $F_x > F_y$. Also, both horizontal and vertical stresses are distributed as expected, along with relatively high horizontal stress at the top of the contact surface in Fig. 20a. Moreover, in Fig. 21, we present the extent of the deformation of the foundation by comparing with its initial shape.

The results for normal and tangential tractions on the contact surface are displayed in Fig. 22. Figure 22a shows that the normal traction is gradually increased to the top, resulting in higher normal traction near the top (i.e., $y = 8$).

Fig. 19 Contour plots of the displacements **a** u_{xx} and **b** u_{yy} for a rigid pile contact with an elastic foundation

(a)

(b)
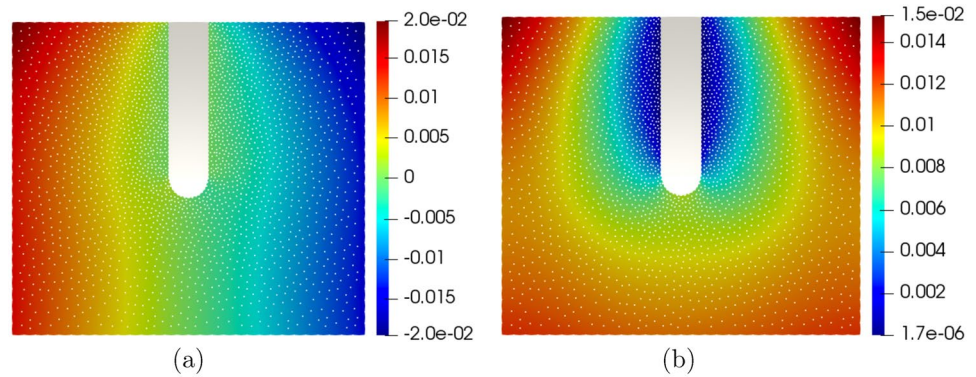
Fig. 20 Contour plots of the stresses **a** σ_{xx} and **b** σ_{yy} for a rigid pile contact with an elastic foundation

(a)

(b)
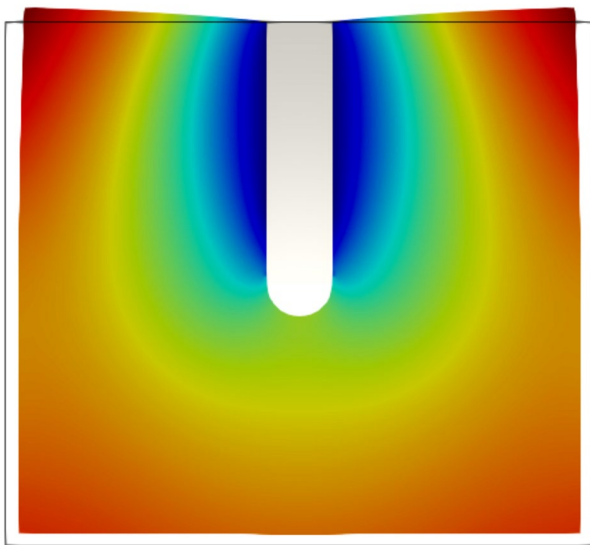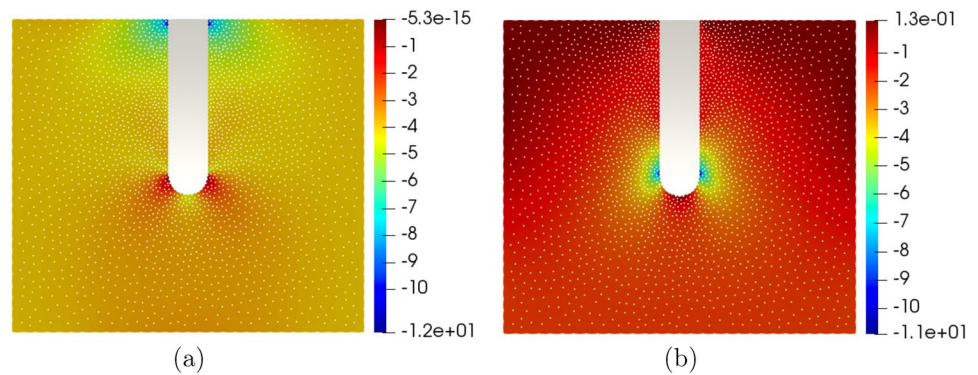
Fig. 21 Comparison of initial and deformed shape for a rigid pile contact with an elastic foundation (a scale factor 15)

5 Conclusion

In this paper, a strong form collocation method formulation has been proposed for the solution of frictional contact problems. The methodology was implemented for two-dimensional problems. The solution algorithm for frictional contact constraints is based on a penalty regularization procedure. A full Newton–Raphson scheme is used to implement the residual form descretized governing equations. The proposed point collocation does not require any type of mesh, which eliminates numerical integration. Furthermore, when compared to other meshfree methods, the proposed point collocation method does require direct calculation of shape function derivatives; resulting in considerable increases in computational speed. Direct discretization of the governing partial differential equations by way of Taylor expansion and moving least squares is a key advantage of the proposed method.

The results from benchmark problems for frictional and frictionless contact problems were provided. The numerical results are compared with conventional finite element method to demonstrate that the methodology is robust and accurate along the contact surface. Results from a comparative analysis between the proposed method and FEM for the 2D elastic slab and a rigid plate problem shows the methods ability to accurately predict the solution field. This problem is often used to validate contact-based algorithms. The corresponding results for 2D elastic block and a rigid cylinder contact problem however considers effects of different Young's Modulus E and load t_x on contact angle. For this problem, the method was able to capture accurate
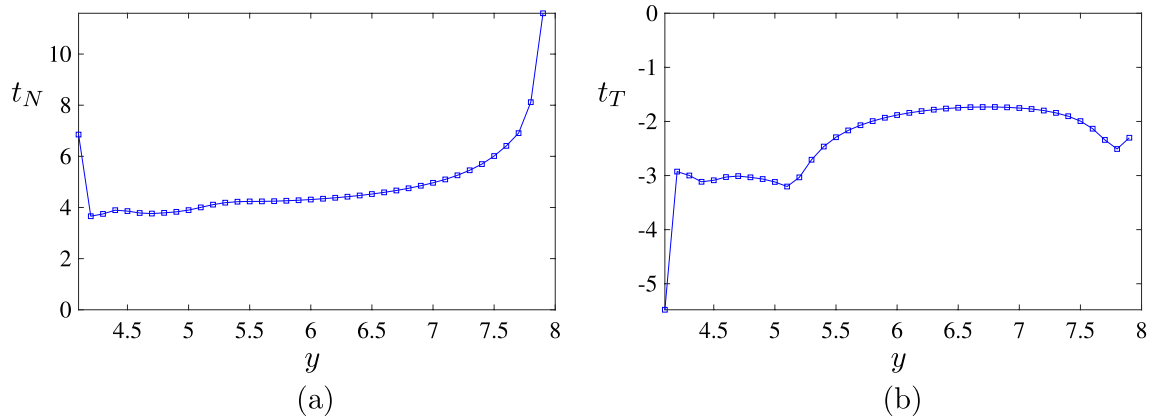
Fig. 22 Contact tractions: **a** normal traction t_N and **b** tangential traction t_T

solutions with minimal local refinement near the contact region thereby significantly reducing computational cost. Finally, we solve a challenging engineering problem which is a contact between rigid pile and an elastic foundation. As expected, high stress concentration is observed in the vicinity of the contact region. In the future, we will apply this method to the large deformation problems to investigate the advantage of the meshless method.

Further verification and theoretical error analyses of the proposed method remains as the authors' future work; a comprehensive review of various formulations and algorithms for the finite element approach within the similar context of contact problems can be found in the literature [47]. Upon successful applications of the proposed method to various Signorini frictional contact problems, our algorithm will be further expended to complex contact problems such as two body frictional contact for inelastic materials [33] in three dimensions [30, 31]. Another obvious interesting future work is to develop an adaptivity algorithm of the proposed method for automatic local refinement.

Appendices

Appendix

The global system of equation can be written

$$
\begin{bmatrix}
K^{int}_{I1J1} & K^{int}_{I2J1} & & & & \\
K^{int}_{I1J2} & K^{int}_{I2J2} & & & 0 & \\
& & K^D_{I1J1} & 0 & & \\
& & 0 & K^D_{I2J2} & & \\
& & & & K^N_{I1J1} & K^N_{I2J1} \\
& & & & K^N_{I1J2} & K^N_{I2J2} \\
& & & & & K^c_{I1J1} & K^c_{I2J1} \\
0 & & & & & K^c_{I1J2} & K^c_{I2J2}
\end{bmatrix}
\begin{bmatrix}
u^{int}_{1I}(\mathbf{x}_I) \\
u^{int}_{2I}(\mathbf{x}_I) \\
u^{D}_{1I}(\mathbf{x}_I) \\
u^{D}_{2I}(\mathbf{x}_I) \\
u^{N}_{1I}(\mathbf{x}_I) \\
u^{N}_{2I}(\mathbf{x}_I) \\
u^{c}_{1I}(\mathbf{x}_I) \\
u^{c}_{2I}(\mathbf{x}_I)
\end{bmatrix}
-
\begin{bmatrix}
-b_1(\mathbf{x}_I) \\
-b_2(\mathbf{x}_I) \\
u_{1I}(\mathbf{x}_I) \\
u_{2I}(\mathbf{x}_I) \\
t_1(\mathbf{x}_I) \\
t_2(\mathbf{x}_I) \\
t_{1c}(\mathbf{x}_I) \\
t_{2c}(\mathbf{x}_I)
\end{bmatrix}
= 0
\tag{53}
$$

The components of K^{int} matrix are

$$
\begin{aligned}
K^{int}_{I1J1} &= [(\lambda + 2\mu)\boldsymbol{\phi}^{(2,0)}_{IJ} + \mu\boldsymbol{\phi}^{(0,2)}_{IJ}], \\
K^{int}_{I2J1} &= (\lambda + \mu)\boldsymbol{\phi}^{(1,1)}_{IJ}, \\
K^{int}_{I1J2} &= (\lambda + \mu)\boldsymbol{\phi}^{(1,1)}_{IJ}, \\
K^{int}_{I2J2} &= \mu\boldsymbol{\phi}^{(2,0)}_{IJ} + (\lambda + 2\mu)\boldsymbol{\phi}^{(0,2)}_{IJ}.
\end{aligned}
\tag{54}
$$

The components of K^D matrix are

$$
K^D_{I1J1} = \boldsymbol{\phi}^{(0,0)}_{IJ}, \quad K^D_{I2J2} = \boldsymbol{\phi}^{(0,0)}_{IJ}.
\tag{55}
$$

The components of K^N matrix are

$$
\begin{aligned}
K^N_{I1J1} &= (\lambda + 2\mu)\boldsymbol{\phi}^{(1,0)}_{IJ}n_1 + \mu\boldsymbol{\phi}^{(0,1)}_{IJ}n_2, \\
K^N_{I2J1} &= \lambda\boldsymbol{\phi}^{(0,1)}_{IJ}n_1 + \mu\boldsymbol{\phi}^{(1,0)}_{IJ}n_2, \\
K^N_{I1J2} &= \mu\boldsymbol{\phi}^{(0,1)}_{IJ}n_1 + \lambda\boldsymbol{\phi}^{(1,0)}_{IJ}n_2, \\
K^N_{I2J2} &= (\lambda + 2\mu)\boldsymbol{\phi}^{(0,1)}_{IJ}n_2 + \mu\boldsymbol{\phi}^{(1,0)}_{IJ}n_1.
\end{aligned}
\tag{56}
$$

The components of K^c matrix for stick case are

$$K^c_{I1J1} = K^N_{I1J1}+, K^{stick}_{I1J1}, \quad K^c_{I2J1} = K^N_{I2J1}+, K^{stick}_{I2J1},$$
$$K^c_{I1J2} = K^N_{I1J2}+, K^{stick}_{I1J2}, \quad K^c_{I2J2} = K^N_{I2J2}+, K^{stick}_{I2J2}, \tag{57}$$

where K^N_{I1J1}, K^N_{I2J1}, K^N_{I1J2}, and K^N_{I2J2} can be obtained from Eq. (56). The component of stiffness matrix K^{stick} in Eq. (57) defined as

$$K^{stick}_{I1J1} = \boldsymbol{\phi}^{(0,0)}_{IJ}H(g(\mathbf{x}_J)) + [\epsilon_N \nu_1 \nu_1 + \epsilon_T \tau_1 \tau_1],$$
$$K^{stick}_{I2J1} = \boldsymbol{\phi}^{(0,0)}_{IJ}H(g(\mathbf{x}_J)) + [\epsilon_N \nu_2 \nu_1 + \epsilon_T \tau_2 \tau_1],$$
$$K^{stick}_{I1J2} = \boldsymbol{\phi}^{(0,0)}_{IJ}H(g(\mathbf{x}_J)) + [\epsilon_N \nu_1 \nu_2 + \epsilon_T \tau_1 \tau_2],$$
$$K^{stick}_{I2J2} = \boldsymbol{\phi}^{(0,0)}_{IJ}H(g(\mathbf{x}_J)) + [\epsilon_N \nu_2 \nu_2 + \epsilon_T \tau_2 \tau_2]. \tag{58}$$

The components of $\mathbf{f}^c_{stick}$ vector are

$$t^c_1(\mathbf{x}_J) = \epsilon_N < g(\mathbf{x}_J) > \nu_1 - \epsilon_T H(g(\mathbf{x}_J))(u_k\tau_k)\tau_1$$
$$t^c_2(\mathbf{x}_J) = \epsilon_N < g(\mathbf{x}_J) > \nu_2 - \epsilon_T H(g(\mathbf{x}_J))(u_k\tau_k)\tau_2.$$

The components of K^c matrix for stick case are

$$K^c_{I1J1} = K^N_{I1J1}+, K^{slip}_{I1J1}, \quad K^c_{I2J1} = K^N_{I2J1}+, K^{slip}_{I2J1},$$
$$K^c_{I1J2} = K^N_{I1J2}+, K^{slip}_{I1J2}, \quad K^c_{I2J2} = K^N_{I2J2}+, K^{slip}_{I2J2}. \tag{59}$$

The component of stiffness matrix K^{slip} in Eq. (59) defined as

$$K^{slip}_{I1J1} = \boldsymbol{\phi}^{(0,0)}_{IJ}H(g(\mathbf{x}_J)) + [\epsilon_N \nu_1 \nu_1 - \mu\epsilon_N \mathrm{sign}(u_k\tau_k)\nu_1\tau_1],$$
$$K^{slip}_{I2J1} = \boldsymbol{\phi}^{(0,0)}_{IJ}H(g(\mathbf{x}_J)) + [\epsilon_N \nu_2 \nu_1 - \mu\epsilon_N \mathrm{sign}(u_k\tau_k)\nu_2\tau_1],$$
$$K^{slip}_{I1J2} = \boldsymbol{\phi}^{(0,0)}_{IJ}H(g(\mathbf{x}_J)) + [\epsilon_N \nu_1 \nu_2 - \mu\epsilon_N \mathrm{sign}(u_k\tau_k)\nu_1\tau_2],$$
$$K^{slip}_{I2J2} = \boldsymbol{\phi}^{(0,0)}_{IJ}H(g(\mathbf{x}_J)) + [\epsilon_N \nu_2 \nu_2 - \mu\epsilon_N \mathrm{sign}(u_k\tau_k)\nu_2\tau_2]. \tag{60}$$

The components of $\mathbf{f}^c_{slip}$ vector are

$$t^c_1(\mathbf{x}_J) = \epsilon_N < g(\mathbf{x}_J) > \nu_1 - \mu\epsilon_N < g(\mathbf{x}_J) > \mathrm{sign}(u_k\tau_k)\tau_1$$
$$t^c_2(\mathbf{x}_J) = \epsilon_N < g(\mathbf{x}_J) > \nu_2 - \mu\epsilon_N < g(\mathbf{x}_J) > \mathrm{sign}(u_k\tau_k)\tau_2.$$

References

1. Hallquist J, Goudreau G, Benson D (1985) Sliding interfaces with contact-impact in large-scale Lagrangian computations. Comput Methods Appl Mech Eng 51(1–3):107–137
2. Simo JC, Wriggers P, Taylor RL (1985) A perturbed Lagrangian formulation for the finite element solution of contact problems. Comput Methods Appl Mech Eng 50(2):163–180
3. Benson DJ, Hallquist JO (1990) A single surface contact algorithm for the post-buckling analysis of shell structures. Comput Methods Appl Mech Eng 78(2):141–163
4. Papadopoulos P, Taylor RL (1992) A mixed formulation for the finite element solution of contact problems. Comput Methods Appl Mech Eng 94(3):373–389
5. Wriggers P, Schröder J, Schwarz A (2013) A finite element method for contact using a third medium. Comput Mech 52(4):837–847
6. Wohlmuth BI (2001) Iterative solvers based on domain decomposition. In: Discretization methods and iterative solvers based on domain decomposition. Lecture Notes in Computational Science and Engineering, vol. 17. Springer, Berlin, Heidelberg. https://doi.org/10.1007/978-3-642-56767-4_2
7. Belgacem FB, Maday Y (1994) A spectral element methodology tuned to parallel implementations. Comput Methods Appl Mech Eng 116(1–4):59–67
8. Belhachmi Z, Bernardi C (1994) Resolution of fourth-order problems by the mortar element method. Comput Methods Appl Mech Eng 116(1–4):53–58
9. Maday Y, Mavriplis C, Patera A (1988) Nonconforming mortar element methods: application to spectral discretizations (No. NASA-CR-181729).
10. Bernardi C, Maday Y, Patera AT (1993) Domain Decomposition by the Mortar Element Method. In: Kaper, H.G., Garbey, M.,Pieper, G.W. (eds) Asymptotic and Numerical Methods for Partial Differential Equations with Critical Parameters. NATO ASI Series, vol 384. Springer, Dordrecht. https://doi.org/10.1007/978-94-011-1810-1_17
11. Belgacem FB, Hild P, Laborde P (1997) Approximation of the unilateral contact problem by the mortar finite element method. Comptes Rendus de l'Academie des Sciences Series I Mathematics 324(1):123–127
12. Belgacem FB, Hild P, Laborde P (1998) The mortar finite element method for contact problems. Math Comput Model 28(4–8):263–271
13. McDevitt T, Laursen T (2000) A mortar-finite element formulation for frictional contact problems. Int J Numer Methods Eng 48(10):1525–1547
14. Puso MA, Laursen TA (2004) A mortar segment-to-segment contact method for large deformation solid mechanics. Comput Methods Appl Mech Eng 193(6–8):601–629
15. Yang B, Laursen TA, Meng X (2005) Two dimensional mortar contact methods for large deformation frictional sliding. Int J Numer Methods Eng 62(9):1183–1225
16. Kim TY, Dolbow J, Laursen T (2007) A mortared finite element method for frictional contact on arbitrary interfaces. Comput Mech 39(3):223–235
17. Yoon Y-C, Song J-H (2014) Extended particle difference method for weak and strong discontinuity problems: part i. Derivation of the extended particle derivative approximation for the representation of weak and strong discontinuities. Comput Mech 53(6):1087–1103
18. Yoon Y-C, Song J-H (2014) Extended particle difference method for weak and strong discontinuity problems: part ii. formulations and applications for various interfacial singularity problems. Comput Mech 53(6):1105–1128
19. Yoon Y-C, Song J-H (2014) Extended particle difference method for moving boundary problems. Comput Mech 54(3):723–743
20. Lancaster P, Salkauskas K (1981) Surfaces generated by moving least squares methods. Math Comput 37(155):141–158
21. Belytschko T, Lu YY, Gu L (1994) Element-free Galerkin methods. Int J Numer Methods Eng 37(2):229–256
22. Lu Y, Belytschko T, Gu L (1994) A new implementation of the element free Galerkin method. Comput Methods Appl Mech Eng 113(3–4):397–414
23. Liu WK, Jun S, Zhang YF (1995) Reproducing kernel particle methods. Int J Numer Methods Fluids 20(8–9):1081–1106
24. Liu WK, Jun S, Li S, Adee J, Belytschko T (1995) Reproducing kernel particle methods for structural dynamics. Int J Numer Methods Eng 38(10):1655–1679
25. Liu W, Li S, Belytschko T (1997) Moving least square kernel Galerkin method±part i: methodology and convergence. Comput Methods Appl Mech Eng 143:422–433

26. Li S, Liu WK (1999) Reproducing kernel hierarchical partition of unity, part i-formulation and theory. Int J Numer Methods Eng 45(3):251–288

27. Li S, Liu WK (1999) Reproducing kernel hierarchical partition of unity, part ii-applications. Int J Numer Methods Eng 45(3):289–317

28. Kim DW, Kim Y (2003) Point collocation methods using the fast moving least-square reproducing kernel approximation. Int J Numer Methods Eng 56(10):1445–1464

29. Lee S-H, Kim K-H, Yoon Y-C (2016) Particle difference method for dynamic crack propagation. Int J Impact Eng 87:132–145

30. Fu Y, Michopoulos JG, Song J-H (2017) Bridging the multi phase-field and molecular dynamics models for the solidification of nano-crystals. J Comput Sci 20:187–197

31. Song J-H, Fu Y, Kim T-Y, Yoon Y-C, Michopoulos JG, Rabczuk T (2018) Phase field simulations of coupled microstructure solidification problems via the strong form particle difference method. Int J Mech Mater Des 14, 491–509. https://doi.org/10.1007/s10999-017-9386-1

32. Almasi A, Beel A, Kim T-Y, Michopoulos JG, Song J-H (2019) Strong-form collocation method for solidification and mechanical analysis of polycrystalline materials. J Eng Mech 145(10):04019082

33. Yoon Y-C, Schaefferkoetter P, Rabczuk T, Song J-H (2019) New strong formulation for material nonlinear problems based on the particle difference method. Eng Anal Bound Elem 98:310–327

34. Beel A, Kim T-Y, Jiang W, Song J-H (2019) Strong form-based meshfree collocation method for wind-driven ocean circulation. Comput Methods Appl Mech Eng 351:404–421

35. Chen J-S, Wang H-P (2000) New boundary condition treatments in meshfree computation of contact problems. Comput Methods Appl Mech Eng 187(3–4):441–468

36. Li G, Belytschko T (2001) Element-free Galerkin method for contact problems in metal forming analysis. Eng Comput 18(1/2):62–78

37. Xiao J, Gama B, Gillespie J Jr, Kansa E (2005) Meshless solutions of 2d contact problems by subdomain variational inequality and mlpg method with radial basis functions. Eng Anal Bound Elem 29(2):95–106

38. De Lorenzis L, Evans J, Hughes TJ, Reali A (2015) Isogeometric collocation: Neumann boundary conditions and contact. Comput Methods Appl Mech Eng 284:21–54

39. Kruse R, Nguyen-Thanh N, De Lorenzis L, Hughes TJ (2015) Isogeometric collocation for large deformation elasticity and frictional contact problems. Comput Methods Appl Mech Eng 296:73–112

40. Weeger O, Yeung S-K, Dunn ML (2017) Isogeometric collocation methods for Cosserat rods and rod structures. Comput Methods Appl Mech Eng 316:100–122

41. Temizer I, Wriggers P, Hughes TJR (2011) Contact treatment in isogeometric analysis with NURBS. Comput Methods Appl Mech Eng 200(9–12):1100–1112

42. Temizer I, Wriggers P, Hughes TJR (2012) Three-dimensional mortar-based frictional contact treatment in isogeometric analysis with NURBS. Comput Methods Appl Mech Eng 209:115–128

43. Hibbitt H, Karlsson B, Sorensen P (2012) Abaqus theory manual, version 6.12. Pawtucket, Rhode Island

44. Renaud C, Feng Z-Q (2003) Bem and fem analysis of Signorini contact problems with friction. Comput Mech 31(5):390–399

45. Kikuchi N, Oden JT (1988) Contact problems in elasticity: a study of variational inequalities and finite element methods, vol 8. SIAM, Philadelphia

46. Almasi A, Kim T-Y, Laursen TA, Song J-H (2019) A strong form meshfree collocation method for frictional contact on a rigid obstacle. Comput Methods Appl Mech Eng 357:112597

47. Christensen P, Klarbring A, Pang J-S, Strömberg N (1998) Formulation and comparison of algorithms for frictional contact problems. Int J Numer Methods Eng 42(1):145–173